High Pressure Stability of Energetic Crystal of Dihydroxylammonium 5,5'-bistetrazole-1,1'-diolate (TKX-50): Raman Spectroscopy and DFT Calculations.

5 AUTHORS, INCLUDING:

Zbigniew Dreger
Washington State University
124 PUBLICATIONS   1,127 CITATIONS

SEE PROFILE

Yuchuan Tao
Florida State University
14 PUBLICATIONS   64 CITATIONS

SEE PROFILE

Boris B. Averkiev
Washington State University
81 PUBLICATIONS   1,191 CITATIONS

SEE PROFILE

High-Pressure Stability of Energetic Crystal of Dihydroxylammonium 5,5′-Bistetrazole-1,1′-diolate: Raman Spectroscopy and DFT Calculations

Zbigniew A. Dreger,*,[†] Yuchuan Tao,[†] Boris B. Averkiev,[†] Yogendra M. Gupta,[†] and Thomas M. Klapötke[‡]

[†]Institute for Shock Physics and Department of Physics and Astronomy, Washington State University, Pullman, Washington 99164-2816, United States

[‡]Department of Chemistry, Ludwig Maximilian University of Munich, Munich, D-81377, Germany

ABSTRACT: The vibrational and structural behavior of a novel, energetic crystal, dihydroxylammonium 5,5′-bistetrazole-1,1′-diolate (TKX-50), was examined over a broad pressure range to elucidate its structural and chemical stability at high pressures. Raman measurements were performed on single crystals compressed to 50 GPa in a diamond anvil cell, and data were obtained over the entire frequency range of TKX-50 Raman activity. The Raman spectroscopy results were complemented by density functional theory (DFT) calculations to provide vibrational mode assignments and to gain insight into pressure effects on the vibrational and crystal response of TKX-50. Several features were observed in Raman spectra measured in the ranges 4−10, 10−13, and 32−36 GPa. We suggest that the changes between 32 and 36 GPa may be associated with a phase transformation. In addition, a number of vibrational modes showed intensity exchange and avoided crossing of vibrational frequency at various pressures, characteristic of the coupling of modes. Despite all these pressure effects, the compression of TKX-50 to 50 GPa and the subsequent release of pressure did not result in any irreversible spectral changes, demonstrating its remarkable chemical stability. DFT calculations, using the PBE functional with an empirical dispersion correction by the Grimme, PBE-D method, were used to calculate pressure effects on Raman frequencies and unit cell parameters. The calculated Raman shifts to 20 GPa are in good overall agreement with the measured shifts over a broad range of frequencies. The calculations also show that TKX-50 exhibits anisotropic compressibility, with a highly incompressible response along the *a* axis. The calculated bulk modulus, a measure of average stiffness, of TKX-50 is significantly higher than the calculated or measured bulk moduli of other energetic crystals. We suggest that the strong intermolecular interactions and the coupling of vibrational modes may potentially contribute to the shock insensitivity of TKX-50. This work demonstrates the robust high-pressure response of TKX-50, making this crystal attractive for practical applications.
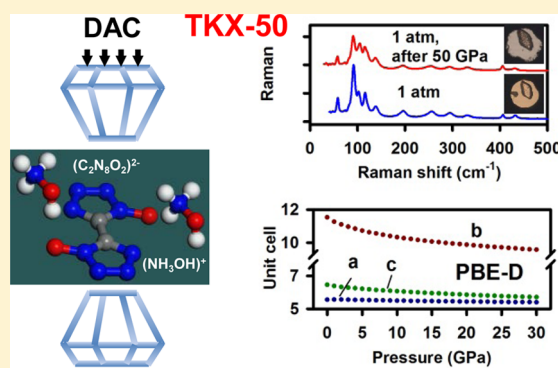
1. INTRODUCTION

There is a continuing need for high-performance, insensitive, and environmentally benign explosives for various military and civil applications. Thus, there have been significant and continuing efforts to obtain high-explosive (HE) crystals that possess these attributes.[1−6] The recently synthesized dihydroxylammonium 5,5′-bistetrazole-1,1′-diolate (TKX-50) is a step forward to meet these needs.[7] TKX-50 is a new azole-based high-performance and low-sensitivity high-explosive crystal that is relatively easy to synthesize from low toxicity components. TKX-50 characteristics are superior to RDX (trimethylene-trinitramine), often used as a benchmark for current high explosives. For example, TKX-50 performance, in terms of detonation velocity, is almost 11% higher, whereas sensitivity to impact is three times lower than RDX. In addition, TKX-50 has a lower toxicity to aquatic life than RDX.[7]

The attractive characteristics of TKX-50 have prompted an interest in understanding the underlying processes governing its properties.[7,8] Among these, the low sensitivity or high stability is of significant interest because of the growing need for safer high explosives. Because many HE applications involve shock-wave compression, an understanding of the high-pressure and high-temperature response of TKX-50 is important for understanding its low impact sensitivity.

Although several properties of TKX-50 have been investigated experimentally[7] and theoretically,[8] its static high-pressure response is completely unknown. Here, we present the first high-pressure studies on TKX-50. We used Raman spectroscopy because vibrational properties are critical for

understanding the strength and stability of intramolecular and intermolecular bonding, molecular interactions, and vibrational coupling. In addition, vibrational studies constitute a useful approach to elucidate the polymorphic[9−15] and reactive behavior[16−19] of HE crystals under the extreme conditions of pressure and temperature. Moreover, we used density functional theory (DFT) calculations in conjunction with the experimental results to gain insight into molecular processes.

TKX-50 crystallizes in the monoclinic space group $P2_1/c$ with two anion−cation moieties in the unit cell.[7] The molecular moiety consists of the bistetrazole anion, $C_2N_8O_2^{2-}$, and two hydroxylammonium cations, NH_3OH^+. The ambient structure is stabilized by an extensive 3D network of intermolecular hydrogen bonding: each hydrogen atom of the cation connects with neighboring cations and anions (Figure 1). There are eight
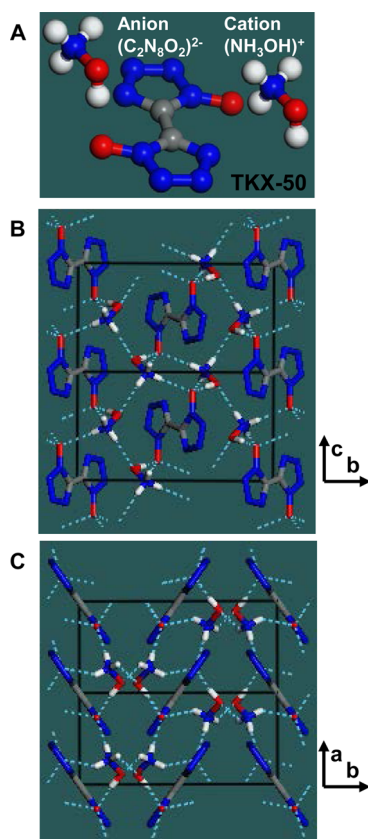

Figure 1. Molecular and crystal structure of TKX-50 at ambient pressure and 100 K.[7] (A) TKX-50 moiety: two cations $(NH_3OH)^+$ and an anion $(C_2N_8O_2)^{2-}$. Projection of two unit cells on the (101) plane (B) and on the (011) plane (C). Molecules are represented either by the ball-and-stick model (A) or by the stick model (B and C). Hydrogen bonds are denoted by blue dashed lines. Legend: carbon, gray; nitrogen, blue; oxygen, red; hydrogen, white. Crystal unit cells are represented by black lines.

different hydrogen bonds: three of each N−H···N and N−H···O type, and single O−H···N and O−H···O bonds. The strength of these bonds can be classified on the basis of the distance between donor and acceptor, $d(D···A)$, and the bond angle, $\angle(D-H···A)$.[7,20] Accordingly, the O−H···O bond can be viewed as the strong one, and the N−H···N bonds, as the weak ones. This large disparity in the H-bond strengths may lead to anisotropy in the intermolecular interactions and may govern the TKX-50 response to high-pressure compression.

In this work, we present comprehensive experimental and theoretical results regarding pressure effects on the vibrational and structural properties of TKX-50. We used Raman spectroscopy and DFT calculations (i) to provide a full assignment of Raman active vibrations, (ii) to examine the high-pressure structural and chemical stability, (iii) to determine changes in molecular vibrations under high pressure to identify the factors that may stabilize the structure, and (iv) to ascertain changes in hydrogen bonding and their role in crystal stability.

The remainder of the paper is organized as follows. Experimental and computational methods are described in the next section. Section 3 presents experimental and computational results and discussions regarding (i) pressure dependence of internal and external vibrations to 50 GPa and unit cell parameters to 30 GPa, (ii) pressure-induced vibrational coupling, and (iii) changes in hydrogen bonding. The main findings of this work are summarized in Section 4.

2. METHODS

2.1. Experiments. TKX-50 single crystals were prepared using the method described in ref 7. The crystals were used as grown but selected on the basis of crystal quality and size to fit the high-pressure compartment.

High pressures were generated using a modified Merrill− Bassett type diamond anvil cell (DAC). A rhenium gasket, preindented to 0.05 mm with a 0.12 mm hole drilled in the indentation, served as the sample compartment. Experiments were performed using cryogenically loaded nitrogen as a pressure transmitting medium. We verified that cryogenic loading did not affect the crystal quality. Frequency shifts of the ruby R lines were used to monitor pressure in the sample compartment. The precision of our pressure measurements was estimated to be 0.05 GPa.

The 532 nm line from a continuum wave diode-pumped solid-state laser was used for Raman excitation. A micro-Raman system (T64000, JY-Horiba) equipped with a microscope (Olympus BX-40) was used for the measurements reported here; it provided a spectral resolution of ∼0.8 cm^{-1} and a spatial resolution of 5 μm. This system was capable of measuring Raman frequencies as low as 20 cm^{-1}. Raman spectra measurements were performed up to 50 GPa. Pressure-induced shifts of overlapping peaks were analyzed by fitting the spectra to a Voigt (Gaussian−Lorentzian) function using a nonlinear least-squares algorithm included in the PeakFit software. Experimental details regarding our Raman and ruby fluorescence techniques can be seen elsewhere.[21]

2.2. Computations. Crystal and vibrational structure calculations were performed using the periodic plane-wave density functional theory (DFT) method with norm-conserving pseudopotential implemented in the CASTEP program.[22] Various density functionals and dispersion-correction schemes were tested for structure calculations at ambient pressure. Both the generalized gradient approximation (GGA) with the Perdew−Burke−Ernzerhof (PBE)[23] and PW91 (Perdew and Wang)[24] functionals, and the local density approximation (LDA) of Ceperley and Alder[25] parametrized by Perdew and Zunger (CA-PZ)[26] were used for the exchange-correlation potentials. To account for the van der Waals (vdW) interactions, we used three types of corrections: to PBE by Grimme (PBE-D)[27] and Tkatchenko and Scheffler (PBE-TS),[28] and to CA-PZ and PW91 by Ortmann, Bechstedt, and Schmidt[29] (CA-PZ-OBS and PW91-OBS). The Brillouin zone

of the reciprocal space of the TKX-50 crystal was sampled by a Monkhorst−Pack grid:[30] $3 \times 1 \times 2$ k points. Such grids provide a minimum k-point separation of 0.07 Å^{-1}. The norm-conserving pseudopotential was used, and the energy cutoff for the basis set was 830 eV. The Broyden−Fletcher−Goldfarb−Shanno (BFGS) algorithm[31] was used to optimize the unit cell parameters and the atomic coordinates simultaneously while keeping the crystal structure symmetry. The convergence criteria for geometry optimization were maximum change in system energy of 5×10^{-6} eV/atom, maximum force of 0.01 eV/Å, maximum stress of 0.02 GPa, and maximum displacement of 5×10^{-6} Å.

3. RESULTS

3.1. Ambient Pressure Response. *3.1.1. Experimental Raman Spectra.* In TKX-50, there are 141 optical modes. For the space group $P2_1/c$ (C_{2h}), a group-theoretical analysis gives the following decomposition into irreducible components: $\Gamma_{\text{inter}} = 33A_g + 33B_g + 33A_u + 33B_u$ (internal) and $\Gamma_{\text{ext}} = 3A_g + 3B_g + 2A_u + B_u$ (external). From these, the modes with inversion symmetry, A_g and B_g, are Raman-active. Thus, there are 33 internal and 3 external Raman vibrations of each symmetry, a total 72 modes.

In Figure 2, we present the Raman spectrum of TKX-50 over a broad frequency range. The spectrum was divided into three
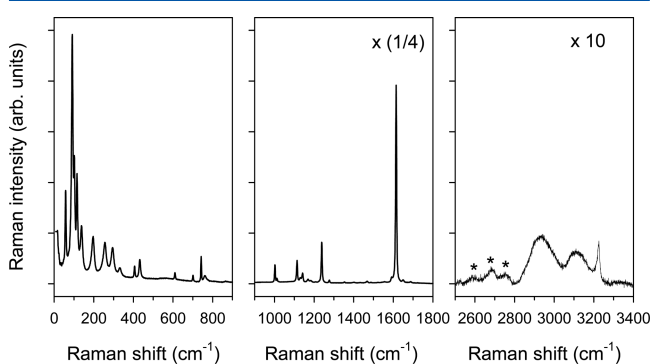

Figure 2. Raman spectra of single crystal of TKX-50 at ambient pressure. Intensities of peaks in the range from 900 to 1800 cm^{-1} were divided by 4, whereas in the range from 2500 to 3400 cm^{-1}, they were multiplied by 10. Asterisks denote peaks of very low intensity that could not be resolved under high pressure.

parts to assist in resolving peaks having different intensities. The intensity of the strongest peak at 1615 cm^{-1} was ∼4 times higher than the intensity of the second strongest peak. The lowest intensity was observed in the high-frequency region, associated with the OH and NH$_2$ stretching vibrations. The frequencies of Raman peaks obtained from the spectra are listed in Table 1, along with their vibrational assignments. Overall, we were able to detect 3 lattice and 34 intramolecular modes. From the latter, 32 modes were assigned to fundamental vibrations and 2 modes to combinations or overtones. The number of observed peaks, fewer than theoretically predicted, is likely due to a weak crystal field effect, preventing the resolution of A_g and B_g modes that are close in frequency.

3.1.2. Calculated Crystal Structure and Raman Frequencies. Before calculating the crystal Raman frequencies, we first examined the ability of the computational approaches to reproduce the experimental crystal structure. Various DFT methods, standard density functionals LDA (CA-PZ), GGA

(PW91), and GGA (PBE) and their corrected versions, were tested for calculating the unit cell parameters. The calculated results are compared with the experimental values in Table 2. As expected, the standard functionals generate large errors because they do not adequately account for the weak interactions in a molecular crystal. The calculated crystal volume is underestimated by −7.8% using the CA-PZ functional and overestimated by 13.0 and 13.3% with the PW91 and PBE functionals, respectively. These discrepancies can, in principle, be reduced by using dispersion corrections.[32] As seen in Table 2, the correction to CA-PZ did not improve calculated results; however, corrections to PW91 and PBE functionals provided significant improvements. The errors in the calculated volumes were reduced to −1.3, 5.8, and 0.02%, respectively, for PW91-OBS, PEB-TS, and PBE-D. Furthermore, the PBE-D method reproduces very well the experimental unit cell parameters: all calculated values are within 1% of the experimental data.

Raman frequencies were initially calculated at the Γ point using a finite displacement method and the PBE functional with empirical correction (PBE-D). This approach was used recently for FOX-7 (1,1-diamino-2,2-dinitroethene), providing a very good prediction of the experimental data.[33] Unfortunately, as shown in Figure 3, this approach did not work well for TKX-50; the calculated results were in significant disagreement with the experimental data. For example, the calculated spectrum has a strong peak at about 520 cm^{-1}, which is not observed in the experiment. In addition, the calculations do not predict the experimentally observed feature at about 3100 cm^{-1}.

Therefore, we calculated the vibrational frequencies using the standard PBE functional with a Monkhorst−Pack k point grid, using unit cell parameters obtained from the PBE-D calculations. The atomic coordinates were reoptimized in the PBE method, and vibrational frequencies were calculated for the reoptimized structure using a linear response approach. Selected calculated spectra using the above approach are compared with the experimental data in Figure 3. As seen, this approach provided quite good agreement with the experiments, in particular in the low-frequency range. Differences between calculated and experimental peaks in the high-frequency range likely result from two factors. First, the experimental peaks in this range are broad as a result of the involvement of these modes in hydrogen bonding. The calculations do not account for this broadening because the same Lorentzian broadening of 6 cm^{-1} was used for all computed frequencies. Second, the experimental spectrum is composed of fundamental, combination (3096 cm^{-1}), and overtone (3228 cm^{-1}) modes. The latter are not observed in the calculated spectrum because normal mode calculations were performed.

A full set of calculated results is presented in Table 1, along with the results obtained from the LDA (CA-PZ) calculations and from the experiments. A careful inspection of Table 1 shows that both methods provide reasonable agreement with the experimental data. In particular, we notice that the PBE method, for the PBE-D cell parameters, better reproduces the range of low frequency, 0−800 cm^{-1}, and of high frequency, above 2900 cm^{-1}, whereas the LDA method performs better for the intermediate frequencies, 900−1700 cm^{-1}.

An examination of the atomic motions reveals that Raman modes of TKX-50 are a combination of different vibrations delocalized over the molecule and can, in general, be categorized into three groups. The low frequency modes up to ∼200 cm^{-1} are due to collective vibrations of anions and

Table 1. Characteristics of Raman Active Vibrations in TKX-50 Crystal at Ambient Pressure and Pressure Dependencies of Frequencies

| | frequency (cm^{-1}) | | | assignment | | | $d\nu/dp$ cm^{-1} GPa^{-1} | |
| | | calcd | | | vibration | | | |
mode no.[a]	exptl	GGAPBE	LDA CA-PZ	sym.	$(C_2N_8O_2)^{2-}$	$(NH_3OH)^+$	exptl	calcd
1	58	58	71	A$_g$	rock (in-plane rotation)	rotation	7.2	6.0
2		62	77	B$_g$				
3	92	99	108	A$_g$	twist	rotation	8.5	6.6
4	103	119	130	B$_g$	wag	rotation	6.0	4.1
5		117	114	A$_g$	wag	translation		
6		115	126	B$_g$	twist, wag	rotation		
7	116	130	133	A$_g$	wag	translation	9.2	5.1
8	122	130	133	B$_g$	twist	rock	7.6	14.2
9		155	145	A$_g$	wag	rock		
10	138	168	154	B$_g$		translation	9.1	11.9
11	196	204	226	A$_g$	twist	rotation	5.5	6.2
12		205	237	B$_g$				
13	220	224	265	A$_g$		rock	12.7	17.8
14		240	260	B$_g$				
15	256	264	290	A$_g$		NH$_3$ rotation	12.0	14.2
16		264	285	B$_g$				
17		283	298	B$_g$	ring twist, wag	NH$_3$ rotation		
18		273	299	A$_g$				
19	295	311	332	A$_g$	ring rock, N−O rock	NH$_3$ rotation	10.6	14.9
20		303	311	B$_g$				
21	332	341	366	A$_g$	C−C wag, ring wag	NH$_3$ rotation	9.0	13.3
22		345	375	B$_g$				
23	406	406	411	A$_g$	C−C st, ring in-plane shifting		2.7	2.8
24		405	419	B$_g$				
25	433	431	461	A$_g$	C−C wag; N−O, ring wag		4.5	3.6
26		426	452	B$_g$				
27	610	599	615	A$_g$	ring in-plane rock		2.8	2.1
28		599	614	B$_g$				
29	701	661	681	A$_g$	C−C wag., ring distort[b]		1.2	1.0
30		662	682	B$_g$				
31	742	715	732	A$_g$	C−C wag, ring distort[c]		0.2	−0.1
32		715	732	B$_g$				
33	761	760	782	A$_g$	ring distort[d]	O−H wag	4.1	3.3
34		760	782	B$_g$				
35		874	939	A$_g$		O−H wag		
36		880	945	B$_g$				
37	1002	966	988	A$_g$	C−C rock in-plane, ring distort[e]		2.9	2.6
38		968	990	B$_g$				
39	1013	1018	1055	A$_g$		N−O str.and breath	6.0	4.6
40		1020	1062	B$_g$				
41	1114	1073	1118	A$_g$	ring distort[f]		4.8	5.0
42		1073	1120	B$_g$				
43	1131	1099	1140	A$_g$	ring distort[g]		5.8	3.4
44	1142	1100	1141	B$_g$			5.5	3.4
45	1169	1159	1144	A$_g$		NH rock, OH rock	−2.9	−2.4
46		1165	1153	B$_g$				
47	1183	1200	1226	A$_g$	ring distort[h]		9.5	8.0
48		1206	1236	B$_g$				
49	1239	1206	1241	A$_g$	ring distort[h]		4.3	7.2
50		1210	1243	B$_g$				
51	1277	1256	1281	A$_g$	in-plane C−C rock, complex ring distort		3.5	3.3
52		1263	1290	B$_g$				
53	1468	1432	1458	A$_g$	in-plane C−C rock, ring distort[j]		5.9	4.2
54		1438	1469	B$_g$				
55	1486	1520	1471	A$_g$	in-plane C−C rock, ring distort[j]	NH rock, OH rock	0.9	−2.1
56		1529	1491	B$_g$				

Table 1. continued

	frequency (cm^{-1})				assignment			dν/dp cm^{-1} GPa^{-1}	
		calcd				vibration			
mode no.^{a}	exptl	GGAPBE	LDA CA-PZ	sym.	$(C_2N_8O_2)^{2-}$		$(NH_3OH)^+$	exptl	calcd
57	1591	1560	1507	A$_g$			NH rock, OH rock	−2.3	−4.1
58		1565	1520	B$_g$					
59	1593	1570	1555	B$_g$	C−C str		NH rock, OH rock	6.1	8.1
60		1567	1552	A$_g$					
61	1615	1584	1620	A$_g$	C−C str		NH rock, OH rock	6.4	5.5
62		1583	1621	B$_g$					
63	1650	1596	1539	B$_g$			NH$_2$ scissor, NH rock, OH rock	7.2	4.0
64		1594	1542	A$_g$					
65		2658	2462	A$_g$			NH asym str, OH asym str		
66		2661	2464	B$_g$					
67	2931	2905	2892	A$_g$			NH sym str, OH sym str	5.3	7.8
68		2907	2891	B$_g$					
69	3096				comb (1486 + 1615)			−0.6	
70	3170	3150	3053	A$_g$			NH$_2$ sym str	−2.4	−7.4
71		3154	3047	B$_g$					
72	3216	3231	2971	A$_g$			NH$_2$ asym str	−4.4	−26.5
73		3246	3022	B$_g$					
74	3228				overtone (2 × 1615)			13.5	

^{a}Modes denoted by the bold font were observed experimentally. ^{b}Half-chair, out-of-plane. ^{c}Envelope, out-of-plane. ^{d}Ring stretching. ^{e}C−N′ (N′ atom bonded with O), N=N−N scissor, in-plane. ^{f}N=N stretching, N−N and N−N′ stretching, in-plane. ^{g}N−N stretching, N−N′ stretching opposite, in-plane. ^{h}N=N−N′ sym. stretching, in-plane. ^{j}C−C−N′ scissor, in-plane. Abbreviations: rock = rocking; wag = wagging; twist = twisting; distort = distortion; stretch = stretching; sym = symmetric; asym = asymmetric. Vibrations in C$_2$N$_8$O$_2^{2-}$ are labeled as follows: rocking, in-plane vibration (C−C bond is perpendicular to the axis of rotation); twisting, out-of-plane vibration (C−C bond is the axis of rotation); and wagging, out-of-plane vibration (C−C bond is perpendicular to the axis of rotation).

Table 2. . Experimental and Calculated Unit Cell Parameters of TKX-50 at Ambient Pressure^a

		calcd						
		LDA		GGA				
parameters	exptl^b	CA-PZ	CA-PZ OBS	PW91	PW91 OBS	PBE	PBE TS	PBE-D
a (Å)	5.487	5.525	5.483	5.062	5.459	5.084	5.137	5.537
b (Å)	11.547	11.048	10.580	13.136	11.594	13.148	12.416	11.519
c (Å)	6.483	6.216	6.087	6.992	6.417	6.977	6.821	6.448
β^0	95.40	96.33	97.16	96.53	96.29	96.36	96.15	96.11
V (Å^3)	408.97	377.15	350.33	461.95	403.71	463.48	432.53	408.90

^{a}Calculated values were obtained for various exchange-correlation functionals. ^{b}Ref (results obtained at 100 K).

cations and, thus, are attributed either to external (lattice) modes or to their mixture with low-frequency molecular vibrations. Intermediate modes (200−1650 cm^{-1}) are assigned to different distortions of the anion ring and to contributions from the NH$_3$ rotations and OH wagging vibrations of the cation. The highest-frequency modes (above 1650 cm^{-1}) are controlled by the NH and OH rocking as well as by the NH$_2$ and OH stretching vibrations. Furthermore, we found that the calculated frequencies of A$_g$ and B$_g$ symmetry were quite close, and the A$_g$ vibrations usually had a higher Raman intensity than the corresponding B$_g$ vibrations. Because of this feature, the majority of the experimentally observed modes were found to have the A$_g$ symmetry.

3.2. High Pressure Experiments. *3.2.1. Chemical and Structural Stability: Raman Spectra.* The effect of pressure on TKX-50 Raman frequencies, below 1900 cm^{-1}, is presented in Figures 4 and 5. Figure 4 shows the Raman spectra at several pressures; Figure 5 displays the pressure shifts of the Raman peaks. With increasing pressure, several spectral features are observed: (i) blue shift of peaks, except for the mode ν$_{45}$ and

ν$_{57}$; (ii) a decreased sensitivity to pressure of several modes between 4 and 10 GPa; (iii) emergence or disappearance of a few peaks between 10 and 13 GPa; (iv) appearance of several new peaks between 32 and 36 GPa; and (v) apparent coupling of various modes. Despite these pressure-induced changes, the pattern and intensity of the Raman peaks were fully reversible after a complete release of pressure; note the top and bottom spectra in Figure 4. This result shows that neither the pressure increase to 50 GPa (highest pressure reached in this work) nor the subsequent release of pressure to 1 atm caused any measurable irreversible changes, demonstrating the chemical stability of TKX-50 over a large pressure range. Such pressure stability is quite remarkable for a molecular crystal and is in accord with its low sensitivity. This behavior is similar to that reported for FOX-7, another insensitive HE (IHE) crystal.[12] These results suggest that chemical stability over a broad pressure range can be a characteristic of IHE crystals.

Next, we discuss the Raman spectra features that appeared at different pressures. To quantify changes in the vibrational modes, pressure dependences of the Raman shifts (dν/dp,
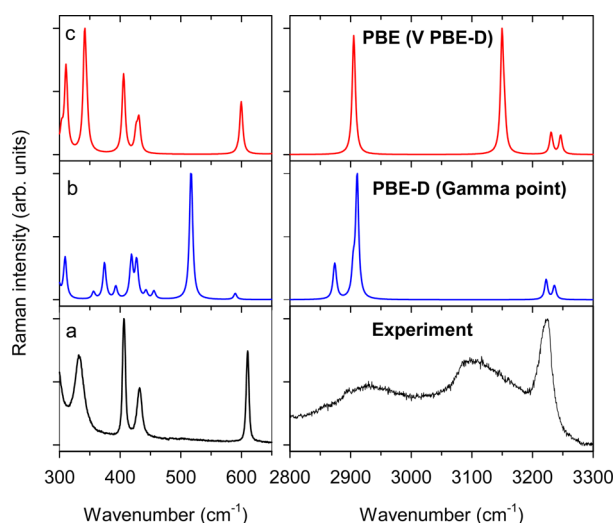
Figure 3. Comparison of selected experimental and calculated Raman spectra of TKX-50 crystal at ambient pressure: (a) experiment, (b) calculations using PBE-D functional with Gamma point, and (c) calculations using the PBE functional and volume calculated with the PBE-D method, labeled as PBE (V PBE-D). The calculated spectra were simulated by applying a Lorentzian broadening of 6 cm^{-1} to the computed frequencies. The intensities in each panel were normalized to the intensity of the strongest peak. Experimental spectra were not corrected for the detector spectral sensitivity.
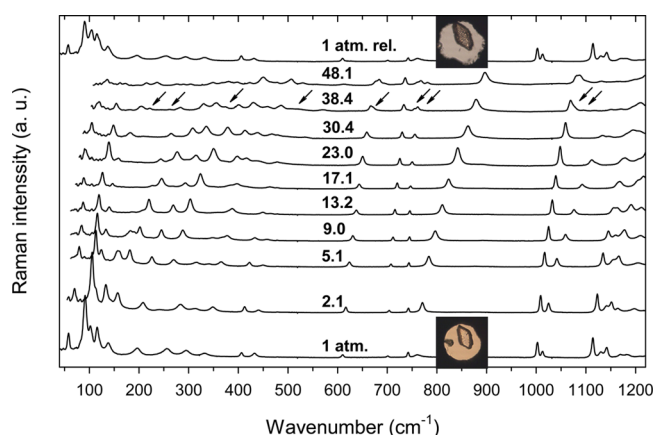
Figure 4. Raman spectra of TKX-50 crystal at several pressures in the frequency range from 50 to 1200 cm^{-1}. Pressure values are given in GPa next to each spectrum. The intensities of spectra at and above 23 GPa were multiplied by 2. Arrows indicate occurrence of new peaks. The top spectrum was measured at ambient pressure after release of pressure from 50 GPa. Images show the TKX-50 crystal in a diamond anvil cell at 1 atm before compression and after release from compression to 50 GPa.

Figure 5. Pressure-induced shifts of Raman peaks in the frequency range from 50 to 1900 cm^{-1}. Experimental results represented by solid points are connected with lines to guide the eye. The mode assignments and their pressure slopes can be found in Table 1. Shift of modes ν_{49} and ν_{51} were not resolved above 1320 cm^{-1} due to their overlapping with a strong diamond peak. The shaded vertical bar denotes the pressure range corresponding to spectral changes.

pressure coefficient) were determined from the least-squares fits of polynomials to experimental data. The calculated coefficients, at ambient pressure, are presented in Table 1. Examination of the table indicates that the pressure coefficients for frequencies below 1900 cm^{-1} vary from −2.9 to 12.7 cm^{-1} GPa^{-1}. The highest positive values are observed for the low frequency modes, including the external modes. However, in contrast to what one would expect, the highest coefficients are not observed for the external modes. This result indicates that intermolecular interactions in TKX-50 may be stronger than in a typical energetic crystal, RDX.[14]
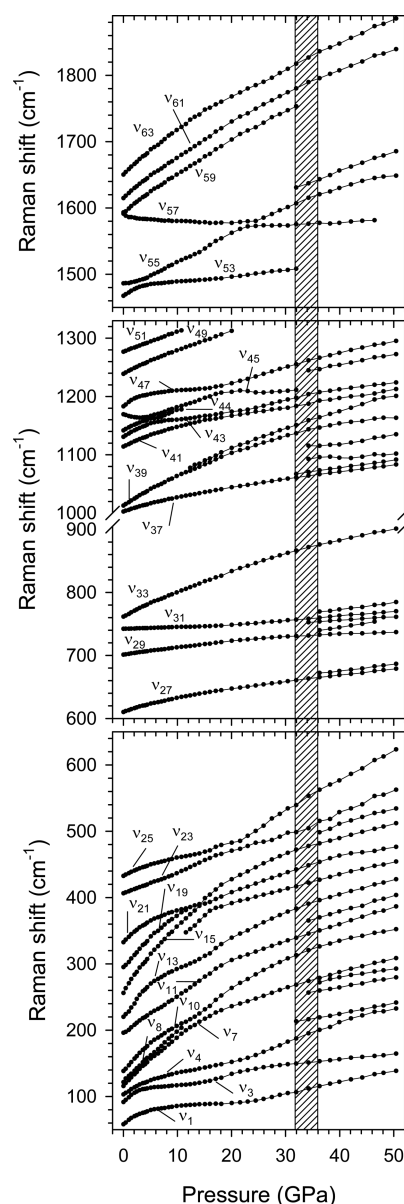
Raman spectra and their analyses are discussed next in three different pressure ranges: 4−10, 10−13, and 32−36 GPa. Between 4 and 10 GPa, several external (ν_1, ν_3, and ν_4) and internal (ν_{13} and ν_{21}) modes show a decreased sensitivity to pressure. Such behavior can likely be a manifestation of structural hardening. Because the affected vibrations are the vibrations corresponding to the entire cation or vibrations of cation bonds, we conjecture that hardening may be caused by the increased confinement of cations. Apparently, the initial pressure increase locks in the cations in their environment, thus slowing down their further adjustment at higher pressures. The proposed scenario seems to be consistent with the observed changes in the behavior of NH$_2$ stretching vibrations at the same pressures. As shown in the next section, there is a gradual

reversal in pressure shifts of these modes from a red to a blue shift. This change can result from the fact that the H-bonds between the anion and cation (N−H···N and N−H···O) experience repulsions from the surrounding neighbors in the crystal confinement, preventing further expansion of the covalent N−H bonds.[34] The vibrational changes observed between 4 and 10 GPa, as described above, do not seem to manifest a phase transition. The gradual character of the spectral changes, the extent of changes over a broad pressure range, the very limited number of modes affected, and the absence of changes in the remaining modes are characteristics of a structural adjustment instead of a phase change. High-pressure X-ray diffraction studies are required for conformation.

Between 10 and 13 GPa, three modes vanish (ν_8, ν_{19}, and ν_{44}), and two modes emerge (below the mode ν_{15} and above the mode ν_{39}). A careful inspection of the spectra indicates that the vanishing modes are actually the modes that merge with the nearby modes as a result of differences in pressure shifts. Thus, they are buried under the stronger adjacent peaks. Furthermore, the examination of two emerging peaks indicates that they show up between the modes ν_{13} and ν_{15}, and ν_{39} and ν_{41}, all of which are the A_g modes. However, we notice that in these frequency regions, theory predicts two additional B_g modes, denoted as ν_{14} and ν_{40}, in Table 1. Hence, we conjecture that the two new peaks could, in fact, be these two B_g modes, which are not observed at lower pressures because of the low intensity or overlapping with the A_g modes. These remarks signify that the spectral changes between 10 and 13 GPa are also not associated with a phase transition.

The last set of spectral changes is observed between 32 and 36 GPa. In this range, a large number of new peaks emerge across all frequencies. In addition, two peaks, ν_{45} and ν_{53}, disappear. This behavior can potentially manifest as a structural phase transition. Because some of new peaks develop gradually with increasing pressure and because they show up in the vicinity of the original modes, nonhydrostatic conditions likely contribute to this transition. The observed considerable increase in the ruby lines width and separation have evidenced the presence of nonhydrostatic compression above 30 GPa. At present, we could not quantify the magnitude of non-hydrostaticity in terms of pressure gradients or deviatoric stresses.

In summary, we linked the observed changes in the Raman spectra in three pressure regions to different crystal and experimental aspects. From our observations and at the present time, only the changes between 32 and 36 GPa can potentially be related to a phase transition. Thus, we infer that TKX-50 can maintain the ambient structure over a broad pressure range, up to 32 GPa. This finding, together with its chemical stability at least to 50 GPa, suggests a very robust response of TKX-50 to high pressure.

3.2.2. Coupling of Modes. Examination of Table 1 indicates that some TKX-50 modes are combinations of both cation and anion vibrations at ambient conditions. This mixed character of the modes changes under pressure because we observed several instances of intensity exchange between various modes and avoided crossing of frequencies with increasing pressure. As seen in Figure 5, this behavior is observed for the following pairs of modes having A_g symmetry: ν_{23}−ν_{25}, ν_{43}−ν_{45}, ν_{45}−ν_{47}, ν_{53}−ν_{55}, and ν_{55}−ν_{57}. In Figures 6 and 7, we show further details to illustrate this behavior. Figure 6 shows the evolution of modes ν_{53} and ν_{55}. As seen, the initially low-intensity mode ν_{55} is gaining intensity while shifting with pressure to higher
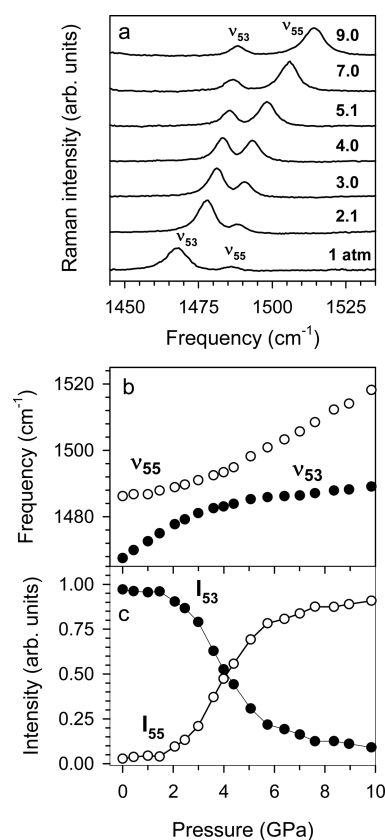

Figure 6. Evolution of Raman peaks ν_{53} and ν_{55} with pressure: (a) spectra at several pressures, (b) peaks shift, and (c) normalized intensity of peaks. The intensity of each peak was divided by the sum of two peaks' intensity; lines are drawn to guide the eye.

frequency and approaching the frequency of the high-intensity mode ν_{53}. Around 4 GPa, the frequencies of two modes differ by about 10 cm^{-1}, and their intensities equalize. With further pressure increase, the frequencies diverge, and the ν_{55} intensity is stronger than the ν_{53} intensity.

In Figure 7, we show another example of modes' interactions. The interactions are complex because of the involvement of several modes. At ambient conditions, there are four modes in the frequency range 1120−1240 cm^{-1}. As the pressure increases, mode ν_{45} interacts with the other modes. Initially, mode ν_{45} shifts to a lower frequency and the two nearby modes, ν_{44} and ν_{43}, shift to higher frequencies. Around 4−6 GPa, the three modes reach close proximity, and their intensities become comparable. Further pressure increase results in an increase in the frequency and the intensity of mode ν_{45}; however, as this mode approaches the low intensity mode ν_{47}, it again loses intensity. Finally, above ~20 GPa, the separation between the two modes increases; mode ν_{47} is significantly more intense than mode ν_{45}.

The above examples show intensity exchange and avoided frequency crossing between the different modes of TKX-50 under high pressure. This behavior is characteristic of the resonance coupling between the modes and is similar to that reported for FOX-7.[12] As shown in the previous work, such coupling can be described in terms of a Fermi resonance model. In the model, the coupling strength between the interacting modes is defined by the Fermi resonance parameter, W.[35] The value of W can be evaluated from the difference between the measured frequencies, δ, at the exact resonance, that is, at the
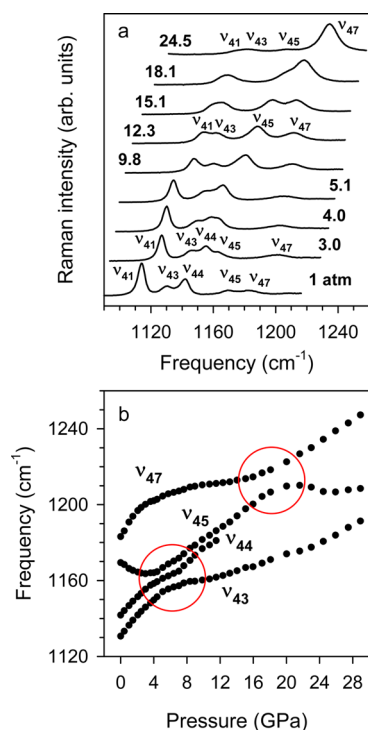
Figure 7. Evolution of Raman peaks in the frequency range from 1100 to 1200 cm^{-1} with pressure: (a) spectra at several pressures and (b) peaks shift. Red circles indicate the pressure regions of mode ν_{45} interaction with other modes.

pressure where the unperturbed frequencies would cross. Thus, $W = \delta/2$, yielding for the modes discussed above: 4.9 cm^{-1} ($\nu_{53}-\nu_{55}$, at ~4.0 GPa), 5.9 cm^{-1} (for $\nu_{45}-\nu_{47}$, at ~18 GPa), and 6.3 cm^{-1} ($\nu_{43}-\nu_{45}$, at ~5.8 GPa). The last value is likely affected by the presence of mode ν_{44}. These values are somewhat higher than the typical value reported for FOX-7 (4.65 cm^{-1}).[12] This suggests that the modes coupling in TKX-50 is somewhat stronger than in FOX-7. Because the coupling in TKX-50 is mostly observed between modes, for which vibrations are localized on two separate molecules, cation and anion, the stronger coupling in TKX-50 could be due to the stronger intermolecular interaction in this crystal than in FOX-7. The observed coupling of modes implies that the vibrations in TKX-50 become further delocalized under high pressure and may have potential implications for the shock insensitivity of TKX-50. As suggested in our work on FOX-7,[12] the vibrational coupling may make it difficult to localize the shock energy needed to initiate bond breaking and a chemical reaction.

3.2.3. Hydrogen Bonding: Frequency Range 2850−3400 cm^{-1}. The ambient structure of TKX-50 is maintained as a result of the extensive network of intermolecular hydrogen bonds. Thus, hydrogen bonding under high pressure is of special interest because it can provide insight into the stability of this crystal at extreme conditions. Hydrogen bonding changes were examined by monitoring changes in the NH and OH stretching vibrations. In TKX-50, there are three experimentally observed modes associated with these vibrations: two NH$_2$ modes, $\nu_{70} = 3170$ and $\nu_{72} = 3216$ cm^{-1}, and one mode with mixed NH and OH character, $\nu_{67} = 2931$ cm^{-1}. Pressure effects on these modes are presented in Figure 8. As pointed out in section 3.1.1, the Raman intensity of these modes is significantly lower than the intensity of the other modes. Furthermore, the peaks of these modes are relatively
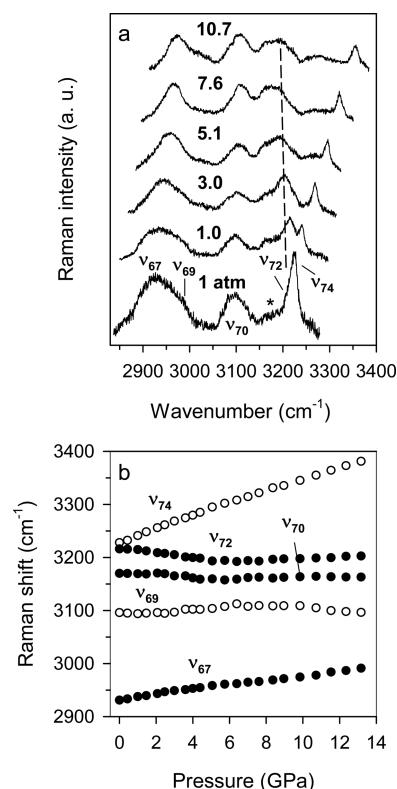

Figure 8. Pressure effect on modes in the frequency range from 2850 to 3400 cm^{-1}. (A) Raman spectra at several pressures. Pressure values are given in GPa next to each spectrum. Assignments of peaks are given in Table 1. The asterisk indicates the background peak. The dashed line is used to help guide the evolution of the ν_{72} mode. (B) Pressure-induced shifts of Raman peaks. Open circles denote peaks assigned to the combination, ν_{69}, and overtone, ν_{74}, modes.

broad and overlap with modes ν_{69} and ν_{74}, which are the combination and overtone modes, respectively (Table 1). Despite this, we were able to follow the evolution of the stretching modes to 14 GPa. As seen in Figure 8, panel b, the two NH$_2$ stretching vibrations, symmetric and asymmetric, show similar dependence with pressure. Frequencies of both modes decrease with an initial pressure increase. This behavior can be attributed to the lengthening of the N−H covalent bonds as a result of the strengthening of the associated hydrogen bonds (N−H···N and N−H···O); however, around ~5 GPa, the initial red shift reverts gradually to a blue shift. The blue shift above 5 GPa, as pointed out earlier, may result from the interactions of H-bonded molecules with the surrounding neighbors, which prevent further lengthening of the covalent N−H bonds.

In contrast to the NH$_2$ stretching modes, the third hydrogen-bonding-related mode, ν_{67}, shows only frequency increase with pressure. Such behavior is characteristic of hydrogen bonds that are relatively strong or are strongly confined by the surrounding molecules.[34] An examination of the TKX-50 ambient crystal structure indicates that both factors may contribute to the observed pressure dependence of mode ν_{67} (see Figure 1).[7] This mode is composed of N−H and O−H bonds vibrations, from which the O−H bond participates in the relatively strong hydrogen bond, with short donor−acceptor distance, d(O−H···O) = 0.26 nm, and angle close to 180°, $\angle$(O−H···O) = 169°.[7] In addition, the H···O bonded cations and anions seem to be tightly confined by nearby molecules.

Overall, the examination of the NH$_2$, NH, and OH stretching vibrations indicate strengthening of the weak H-bonds (N—H···N and N—H···O) and further stabilization of the strong H-bond (O—H···O) under high pressure. Because there were no other spectral features in the pressure range examined, this result implies that beside the hydrogen bonds strengthening, the ambient network of hydrogen bonds is maintained at high pressures.

3.3. High Pressure Calculations. To gain further insight into the high-pressure response of TKX-50, we calculated the pressure dependence of vibrational frequencies and unit cell parameters. As shown below, the calculations reproduce the vibrational frequencies shifts quite well. This agreement lends confidence to the calculated unit cell parameters under pressure.

3.3.1. Pressure Effects on Raman Spectra. Similarly to ambient pressure calculations, the pressure dependencies of vibrational frequencies were calculated using the unit cell parameters obtained from the PBE-D method and frequencies from the standard PBE functional with Monkhorst—Pack k-point grid. The use of this approach for describing pressure effects on vibrational frequencies was evaluated by examining the calculated results with experimental data in Table 1 and Figure 9. It can be seen that the calculated and experimental ambient-pressure coefficients are, in most cases, in relatively good agreement. The calculations correctly predict the sign of the pressure coefficients. Detailed comparisons between the calculated and experimental Raman shifts are presented in Figure 9. To facilitate this comparison, the calculated frequencies at all pressures were shifted by the same amount so that the calculated and experimental values match at ambient pressure. Selected modes are presented to examine the ability to calculate the diverse pressure dependencies.

First, we note that the calculations account well for the shifts of external vibrations: ν_1, ν_3, and ν_4 modes. This result is promising when compared with calculations for other HE crystals, for example, FOX-7[33] and RDX.[36] Likely, the intermolecular interactions in TKX-50, stronger than those in the other HE crystals, contributes to a better performance of the DFT calculations for external vibrations. We also note that the calculations reproduce well the different pressure dependences displayed by the large (ν_{33} and ν_{61}) and small (ν_{31} and ν_{47}) shifts. The theory also performs quite well in describing pressure effect on hydrogen bonds. Although the details of experimental pressure dependencies are not exactly reproduced, the general trends are well predicted. For instance, changes from red to blue shifts observed experimentally for several modes (ν_{45}, ν_{57}, ν_{70}, and ν_{72}) are predicted by the calculations, although at somewhat different pressures. Finally, we can see that the calculations properly reproduce the behavior of hydrogen bonds of different strengths: a blue shift for the strong H-bond (ν_{67}, NH, and OH stretching vibrations) and initial red shift for the weak H-bonds (ν_{70} and ν_{72}, NH$_2$ stretching vibrations).

3.3.2. Pressure Effects on Crystal Unit Cell. In Figure 10, we present the calculated pressure effects on the TKX-50 unit cell parameters. The calculations were performed to 30 GPa, with the same ambient space group maintained at all pressures. This approach is in agreement with the fact that our Raman results indicated no phase changes to 32 GPa. We used primarily[37] the GGA (PBE-D) method because it best reproduced the ambient unit cell (Table 2) and pressure dependence of vibrational frequencies (Figure 9).
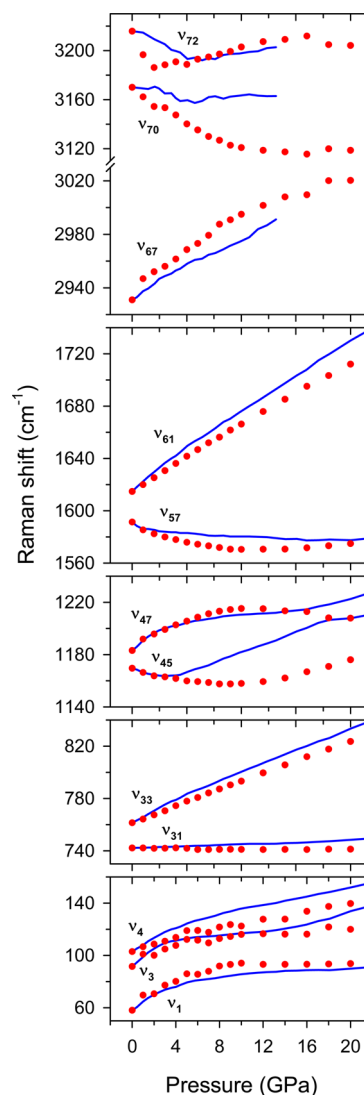

Figure 9. Comparison of experimental (blue lines) and calculated (red solid circles) pressure-induced shifts of selected Raman peaks. Frequencies were calculated with GGA (PBE) for the unit cell parameters obtained from the PBE-D method. Assignment of modes can be found in Table 1

As seen in Figure 10, pressure-induced changes in the unit cell parameters indicate the compressibility of TKX-50 to be highly anisotropic. The relative unit cell parameters, to 30 GPa, were $a/a_0 = 97\%$, $b/b_0 = 83\%$, and $c/c_0 = 88\%$. Thus, TKX-50 appears quite incompressible along the a axis. Initially, this result seems to be quite surprising; however, further examination of the ambient structure (Figure 1) indicates that two factors may contribute to this behavior. First, the intermolecular distances along the a direction are shorter than in other directions. Therefore, the interactions between the molecules are relatively strong, resulting in lower compressibility along the a axis compared with other axes. Second, in the unit cell, the anions and cations are linked together through a network of hydrogen bonds. The strongest H-bonds, i.e., the O—H···O and N—H···O type, have significant components along the a axis.[7]

Our finding of large anisotropic compressibility of TKX-50, with the lowest compressibility along the a axis, is in agreement with the very recent classical force field calculations of impact
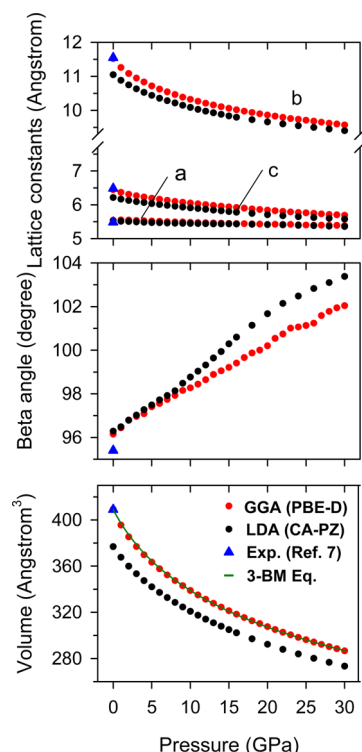
Figure 10. Calculated pressure effects on the unit cell parameters using GGA (PBE-D) (red solid circles) and LDA (CA-PZ) (black solid circles). Experimental results, denoted by blue triangulars, were obtained at ambient pressure and 100 K.[7] A green solid line represents a fit to the GGA (PBE-D) results using the third-order Birch−Murnaghan (3-BM) equation of state.

sensitivity of TKX-50.[38] In that work, large-scale shock simulations indicated different Hugoniot elastic limits (HELs) for three crystallographic directions, with the lowest HEL for the [100] direction. Thus, it was proposed that TKX-50 has anisotropic impact sensitivity, with the [100] direction as least sensitive.

In Figure 10, we also present calculated changes in the unit cell volume. Over the 30 GPa range, the volume reduces to 70%. This reduction in volume appears smaller than the measured or calculated values for other HE crystals. To make a quantitative comparison between TKX-50 and other HE crystals, we compared their bulk moduli. We note that the use of "bulk moduli" as a measure of the average stiffness of strongly anisotropic crystals is not rigorously correct; however, we have compared the bulk moduli in the spirit of the usage in the literature.

We analyzed the TKX-50 results in terms of a semiempirical equation of state (EOS). We applied the third-order Birch−Murnaghan (3-BM) EoS, which is commonly used to evaluate compressibility of solids in a broad range of pressures. The 3-BM EOS equation is as follows:[39]

$$p = \frac{3K_0}{2}\left[\left(\frac{V_0}{V}\right)^{7/3} - \left(\frac{V_0}{V}\right)^{5/3}\right]$$

$$\times \left[1 + \frac{3}{4}(K_0' - 4)\left(\left(\frac{V_0}{V}\right)^{2/3} - 1\right)\right]$$

where K_0 and K_0', respectively, denote the zero pressure isothermal bulk modulus and its pressure derivative, whereas V_0 and V are the unit cell volumes at 1 atm and pressure p.

Fitting this equation to the calculated $p-V$ response, shown in Figure 10, produced K_0 and K_0' values of 31.4 ± 0.3 GPa and 5.6 ± 0.1, respectively. We compare this bulk modulus value with the experimental or calculated bulk moduli for other energetic crystals: PETN-I (12.8 GPa, calcd)[40] and α-RDX (14.9 GPa, calcd);[40] IHE: TATB (17.1 GPa, exptl)[41] and FOX-7 (17.9 GPa, exptl);[42] and ionic HE: TAG-MNT (14.6 GPa, exptl)[43] and G-MNAT (15.3 GPa, calcd).[44] Note that the referred values serve as examples and do not provide a complete list of reported bulk moduli for these materials. From these comparisons, it is clear that TKX-50 is significantly stiffer than the other energetic crystals.

Our previous work has indicated that temperature plays an important role in the initiation and acceleration of decomposition of the shocked RDX crystal.[45] Similarly, if temperature plays an important role in the decomposition of TKX-50, then the following comments are in order. The temperature increase under shock compression is related to the volume change; larger compressibility of a crystal will lead to a higher temperature; thus, the low compressibility of TKX-50, as suggested by our calculation, will result in a smaller temperature rise under shock compression in comparison with other HE crystals. Thus, TKX-50 should initiate at higher stress, in agreement with its low impact sensitivity. Furthermore, the low compressibility of TKX-50 is linked to the presence of strong intermolecular interactions, including H-bonds.

4. SUMMARY

Raman spectroscopy and DFT calculations were used to gain insight into the high-pressure structural and chemical stability of a novel energetic crystal: TKX-50. Raman measurements were obtained on single crystals to 50 GPa, and DFT calculations were carried out to 30 GPa. We present vibrational and symmetry assignments of the Raman modes and pressure-induced changes of the Raman modes. Several new features were observed in the high-pressure spectra: (i) decreased sensitivity to pressure between 4 and 10 GPa for several modes, (ii) appearance or disappearance of peaks between 10 and 13 GPa, (iii) appearance of new peaks between 32 and 36 GPa, and (iv) coupling of several modes at various pressures. From these observations, only the changes between 32 and 36 GPa appear to show features characteristic of a phase transition. Although the structure of the high-pressure phase above 32 GPa was not determined, it seems that nonhydrostatic conditions may contribute to the transition. Despite all of the observed spectral changes, the present results demonstrate that the compression to 50 GPa and subsequent release of pressure did not result in any irreversible spectral changes, implying a remarkable chemical stability of TKX-50 under high pressure.

DFT calculations were used to provide further insight into the vibrational and structural response under high pressure. The experimentally measured vibrational frequencies and their dependence on pressure were well predicted with PBE and CA-PZ functionals in conjunction with the PBE-D method used for calculating the unit cell parameters. The use of the PBE-D approach revealed that the TKX-50 crystal exhibits anisotropic compressibility with a highly incompressible response along the a axis. The anisotropic intermolecular interactions were linked to the shorter intermolecular distances and the stronger hydrogen bonds in the a direction than the two other

directions. The calculated $p-V$ data, fitted to the third-order Birch–Murnaghan equation of state, provided a bulk modulus of 31.4 GPa. This value is considerable higher than the bulk moduli of known energetic crystals, implying strong intermolecular interactions in TKX-50. We conjecture that both the strong intermolecular interactions and the coupling of vibrational modes may potentially contribute to the shock insensitivity of TKX-50.

■ AUTHOR INFORMATION

Corresponding Author
*Phone: 509-335-4233. E-mail: dreger@wsu.edu.
Notes
The authors declare no competing financial interest.

■ ACKNOWLEDGMENTS

■ REFERENCES

(1) Sikder, A. K.; Sikder, N. A Review of Advanced High Performance, Insensitive and Thermally Stable Energetic Materials Emerging for Military and Space Applications. *J. Hazard. Mater. A* **2004**, *112*, 1−15.

(2) Talawar, M. B.; Sivabalan, R.; Anniyappan, M.; Gore, G. M.; Asthana, S. N.; Gandhe, B. R. Emerging Trends in Advanced High Energy Materials. *Comb., Explos., and Shock Waves* **2007**, *43*, 62−72.

(3) Agrawal, J. P. *High Energy Materials: Propelants, Explosives and Pyrotechnics*; Wiley-VCH Verlag GmbH & Co. KGaA: Weinheim, 2010.

(4) Klapötke, T. M. *Chemistry of High-Energy Materials*, 2nd ed.; DeGruyter & Co.: Berlin, 2012.

(5) Talawar, M. B.; Sivabalan, R.; Mukundan, T.; Muthurajan, H.; Sikder, A. K.; Gandhe, B. R.; Rao, A. S. Environmentally Compatible Next Generation Green Energetic Materials (GEMs). *J. Hazard. Mater.* **2009**, *161*, 589−607.

(6) Brinck, T., Ed.; *Green Energetic Materials*; John Wiley & Sons Ltd.: Chichester, UK, 2014.

(7) Fisher, N.; Fisher, D.; Klapötke, T.; Piercey, D. G.; Stierstorfer, J. Pushing the Limits of Energetic Materials — the Synthesis and Characterization of Dihydroxylammonium 5,5′-Bistetrazole-1,1′-diolate. *J. Mater. Chem.* **2012**, *22*, 20418−20422.

(8) An, Q.; Liu, W.-G.; Goddard, W. A., III; Cheng, T.; Zybin, S. V.; Xiao, H. Initial Steps of Thermal Decomposition of Dihydroxylammonium 5,5′-Bistetrazole-1,1′-diolate Crystals from Quantum Mechanics. *J. Phys. Chem. C* **2014**, *118*, 27175−27181.

(9) Baer, B. J.; Oxley, J.; Nicol, M. The Phase Diagram of RDX (Hexahydro-1,3,5-trinitro-s-triazine) under Hydrostatic Pressure. *High Pressure Res.* **1990**, *2*, 99−108.

(10) Gruzdkov, Y. A.; Dreger, Z. A.; Gupta, Y. M. Experimental and Theoretical Study of Pentaerythritol Tetranitrate Conformers. *J. Phys. Chem. A* **2004**, *108*, 6216−6221.

(11) Dreger, Z. A.; Gupta, Y. M. Raman Spectroscopy of High-Pressure−High-Temperature Polymorph of Hexahydro-1,3,5-trinitro-1,3,5-triazine (ε-RDX). *J. Phys. Chem. A* **2010**, *114*, 7038−7047.

(12) Hunter, S.; Sutinen, T.; Parker, S. F.; Morrison, C. A.; Williamson, D. M.; Thompson, S.; Gould, P. J.; Pulham, C. R. Experimental and DFT-D Studies of the Molecular Organic Energetic Material RDX. *J. Phys. Chem. C* **2013**, *117*, 8062−8071.

(13) Dreger, Z. A.; Gupta, Y. M. High Pressure−High Temperature Polymorphism and Decomposition of Pentaerythritol Tetranitrate (PETN). *J. Phys. Chem. A* **2013**, *117*, 5306−5313.

(14) Dreger, Z. A.; Tao, Y.; Gupta, Y. M. High Pressure Vibrational and Polymorphic Response of 1,1-Diamino-2,2-dinitroethene (FOX-7) Single Crystals: Raman Spectroscopy. *J. Phys. Chem. A* **2014**, *118*, 5002−5012.

(15) Hunter, S.; Coster, P. L.; Davidson, A. J.; Millar, D. I. A.; Parker, S. F.; Marshall, W. G.; Smith, R. I.; Morrison, C. A.; Pulham, C. R. High-Pressure Experimental and DFT-D Structural Studies of the Energetic Material FOX-7. *J. Phys. Chem. C* **2015**, *119*, 2322−2334.

(16) Miller, P. J.; Block, S.; Piermarini, G. J. Effects of Pressure on the Thermal Decomposition Kinetics, Chemical Reactivity and Phase Behavior of RDX. *Combust. Flame* **1991**, *83*, 174−184 . (15).

(17) Dreger, Z. A.; Gupta, Y. M. Phase Diagram of Hexahydro-1,3,5-trinitro-1,3,5-triazine Crystals at High Pressures and Temperatures. *J. Phys. Chem. A* **2010**, *114*, 8099−8105.

(18) Dreger, Z. A.; McCluskey, M. D.; Gupta, Y. M. High Pressure-High Temperature Decomposition of γ-Cyclotrimethylene Trinitramine (γ-RDX). *J. Phys. Chem. A* **2012**, *116*, 9680−9688.

(19) Dreger, Z. A. Polymorphism and Decomposition of HE Single Crystals: insight from Static and Shock Compression Experiments. *J. Phys. Conf. Series* **2014**, *500*, 112021−8.

(20) Jeffrey, G. A. *An Introduction to Hydrogen Bonding*; Oxford University Press: Oxford, 1997.

(21) Dreger, Z. A.; Gupta, Y. M. High Pressure Raman Spectroscopy of Single Crystals of Hexahydro-1,3,5-trinitro-1,3,5-triazine (RDX). *J. Phys. Chem. B* **2007**, *111*, 3893−3903.

(22) Clark, S. J.; Segall, M. D.; Pickard, C. J.; Hasnip, P. J.; Probert, M. J.; Refson, K.; Payne, M. C. First Principles Methods Using CASTEP. *Z. Kristallogr.* **2005**, *220*, 567−570.

(23) Perdew, J. P.; Burke, K.; Ernzerhof, M. Generalized Gradient Approximation Made Simple. *Phys. Rev. Lett.* **1996**, *77*, 3865−3868.

(24) Perdew, J. P.; Wang, Y. Accurate and Simple Analytic Representation of the Electron−Gas Correlation Energy. *Phys. Rev. B* **1992**, *45*, 13244−13249.

(25) Ceperley, D. M.; Alder, B. J. Ground State of the Electron Gas by a Stochastic Method. *Phys. Rev. Lett.* **1980**, *45*, 566−569.

(26) Perdew, J. P.; Zunger, A. Self-Interaction Correction to Density-Functional Approximations for Many-Electron Systems. *Phys. Rev. B* **1981**, *23*, 5048−5079.

(27) Grimme, S. Accurate Description of Van der Waals Complexes by Density Functional Theory Including Empirical Corrections. *J. Comput. Chem.* **2004**, *25*, 1463−1473.

(28) Tkatchenko, A.; Scheffler, M. Accurate Molecular Van der Waals Interactions from Ground-State Electron Density and Free-Atom Reference Data. *Phys. Rev. Lett.* **2009**, *102*, 073005−4.

(29) Ortmann, F.; Bechstedt, F.; Schmidt, W. G. Semiempirical Van der Waals Correction to the Density Functional Description of Solids and Molecular Structures. *Phys. Rev. B* **2006**, *73*, 205101−10.

(30) Monkhorst, H. J.; Pack, J. D. Special Points for Brillouin-Zone Integrations. *Phys. Rev. B* **1976**, *13*, 5188−5192.

(31) Pfrommer, B. G.; Cote, M.; Louie, S. G.; Cohen, M. L. Relaxation of Crystals with the Quasi-Newton Method. *J. Comput. Phys.* **1997**, *131*, 233−240.

(32) Sorescu, D. C.; Rice, B. M. Theoretical Predictions of Energetic Molecular Crystals at Ambient and Hydrostatic Compression Conditions Using Dispersion Corrections to Conventional Density Functionals (DFT-D). *J. Phys. Chem. C* **2010**, *114*, 6734−6748.

(33) Averkiev, B. B.; Dreger, Z. A.; Chaudhuri, S. Density Functional Theory Calculations of Pressure Effects on the Structure and Vibrations of 1, 1-Diamino-2,2-dinitroethene (FOX-7). *J. Phys.Chem. A* **2014**, *118*, 10002−10010.

(34) Moon, S. H.; Drickamer, H. D. Effect of Pressure on Hydrogen Bonds on Organic Solids. *J. Chem. Phys.* **1974**, *61*, 48−54.

(35) Herzberg, G. *Infrared and Raman Spectra of Polyatomic Molecules*; D. Van Nostrand: New York, 1945.

(36) Miao, M. S.; Dreger, Z. A.; Winey, J. M.; Gupta, Y. M. Density Functional Theory Calculations of Pressure Effects on the Vibrational Structure of α-RDX. *J. Phys. Chem. A* **2008**, *112*, 12228−12234.

(37) We also used the LDA (CA-PZ) method. As shown in Figure 9, this method underestimates the unit cell parameters across all pressures as compared to GGA (DFT-D).

(38) An, Q.; Cheng, T.; Goddard, W. A., III; Zybin, S. V. Anisotropic Impact Sensitivity and Shock Induced Plasticity of TKX-50 (Dihydroxylammonium 5,5′-bis(tetrazole)-1,1′-diolate) Single Crystals: From Large-Scale Molecular Dynamics Simulations. *J. Phys. Chem. C* **2015**, *119*, 2196−2207.

(39) Birch, F. Finite Elastic Strain of Cubic Crystals. *Phys. Rev.* **1947**, *71*, 809−824.

(40) Landerville, A. C.; Conroy, M. W.; Budzevich, M. M.; Lin, Y.; White, C. T.; Oleynik, I. I. Equations of State for Energetic Materials from Density Functional Theory with Van der Waals, Thermal, and Zero-Point Energy Corrections. *Appl. Phys. Lett.* **2010**, *97*, 251908−1−3.

(41) Stevens, L. L.; Velisavljevic, N.; Hooks, D. E.; Dattelbaum, D. M. Hydrostatic Compression Curve for Triaamino−Trinitrobenzene Determined to 13.0 GPa with Powder X-Ray Diffraction. *Propellants, Explos., Pyrotech.* **2008**, *33*, 286−295.

(42) Peiris, S. M.; Wong, C. P.; Kukljia, M. M.; Zerilli, F. Equation of State and Structural Changes in Diaminodinitroethylene from Experimental Studies and Ab Initio Quantum Calculation. *12th Int. Detonation Symp. Proc.* **2002**, 1−8.

(43) McWilliams, R. S.; Kadry, Y.; Mahmood, M. F.; Goncharov, A. F.; Ciezak-Jenkins. Structural and Chemical Properties of the Nitrogen-Rich Energetic Material Triaminoguanidinium 1-Methyl-5-nitriminotetrazolate Under Pressure. *J. Chem. Phys.* **2012**, *137*, 054501−12.

(44) Babu, K. R.; Vaitheeswaran, G. Structural and Vibrational Properties of Nitrogen-Rich Energetic Material Guanidinium 2-Methyl-5-nitraminotetrazolate. *Chem. Phys. Lett.* **2014**, *592*, 132−137.

(45) Dreger, Z. A.; Gupta, Y. M. Decomposition of γ-Cyclotrimethylene Trinitramine (γ-RDX): Relevance for Shock Wave Initiation. *J. Phys. Chem. A* **2012**, *116*, 8713−8717.